Chen Zhang
Wm Michael Barnes 64 Department of Industrial and Systems Engineering,
Texas A&M University,
College Station, TX 77840-3131
e-mail: chenzhang@tamu.edu

Lei Xue
Department of Materials Science and Engineering,
Texas A&M University,
College Station, TX 77840-3003
e-mail: leixue11@tamu.edu

Kadri C. Atli
Department of Materials Science and Engineering,
Texas A&M University,
College Station, TX 77843
e-mail: catli@tamu.edu

Raymundo Arróyave
Department of Materials Science and Engineering,
Texas A&M University,
College Station, TX 77843
e-mail: rarroyave@tamu.edu

Ibrahim Karaman
Department of Materials Science and Engineering,
Texas A&M University,
College Station, TX 77843
e-mail: ikaraman@tamu.edu

Alaa Elwany[1]
Wm Michael Barnes 64 Department of Industrial and Systems Engineering,
Texas A&M University,
College Station, TX 77843
e-mail: elwany@tamu.edu

On the Fabrication of Defect-Free Nickel-Rich Nickel–Titanium Parts Using Laser Powder Bed Fusion

Laser powder bed fusion (L-PBF) additive manufacturing (AM) is an effective method of fabricating nickel–titanium (NiTi) shape memory alloys (SMAs) with complex geometries, unique functional properties, and tailored material compositions. However, with the increase of Ni content in NiTi powder feedstock, the ability to produce high-quality parts is notably reduced due to the emergence of macroscopic defects such as warpage, elevated edge/corner, delamination, and excessive surface roughness. This study explores the printability of a nickel-rich NiTi powder, where printability refers to the ability to fabricate macro-defect-free parts. Specifically, single track experiments were first conducted to select key processing parameter settings for cubic specimen fabrication. Machine learning classification techniques were implemented to predict the printable space. The reliability of the predicted printable space was verified by further cubic specimens fabrication, and the relationship between processing parameters and potential macro-defect modes was investigated. Results indicated that laser power was critical to the printability of high Ni content NiTi powder. In the low laser power setting ($P < 100$ W), the printable space was relatively wider with delamination as the main macro-defect mode. In the sub-high laser power condition ($100\ W \le P \le 200$ W), the printable space was narrowed to a low hatch spacing region with macro-defects of warpage, elevated edge/corner, and delamination happened at different scanning speeds and hatch spacing combinations. The rough surface defect emerged when further increasing the laser power ($P > 200$ W), leading to a further narrowed printable space. [DOI: 10.1115/1.4054935]

Keywords: laser powder bed fusion (L-PBF), additive manufacturing (AM), nickel-rich nickel–titanium, shape memory alloy (SMA), printability, macroscopic defects, machine learning, rapid prototyping and solid freeform fabrication

1 Introduction

Nickel–titanium (NiTi) is the most common commercially available shape memory alloy (SMA) that exhibits reversible solid phase transformations between martensite and austenite upon temperature or load stimuli [1,2]. On the merits of unique functional properties like shape memory effect (SME) and superelasticity (SE), along with remarkable corrosion resistance and biocompatibility, NiTi SMA has found numerous applications in a variety of industrial sectors such as aerospace [3], automotive [4], biomedical [5,6] in addition to other fields [7,8]. However, fabricating NiTi parts with high degrees of geometric complexity using conventional formative or subtractive manufacturing methods is extremely difficult due to challenges such as accelerated tool wear [9,10], oxidation [11], and poor surface finish [12].

Additive manufacturing (AM) has naturally emerged as a viable alternative to fabricate complex NiTi parts [13,14]. Laser powder bed fusion (L-PBF), as one of the most widely adopted metal AM techniques, has been successfully used to fabricate metallic parts in hard-to-process materials with high degrees of geometric complexity in addition to providing the capability of tailoring microstructural features, mechanical, and functional properties [15,16]. Careful selection of processing parameters such as laser power, scanning speed, hatch spacing, layer thickness, and scanning strategy is essential to enable the fabrication of defect-free parts in L-PBF. Furthermore, through altering these processing parameters, the thermal history within the processed material during fabrication can be modulated to control composition, microstructure, and the resulting mechanical and functional properties [17].

With these capabilities in mind, it is important to point out that L-PBF AM of NiTi does not come without challenges. The material is extremely sensitive to processing conditions and more susceptible to defects and residual stresses than other material systems that were successfully printed in previous studies (e.g., steels and their alloys), particularly for high Ni content compositions [18]. Many research efforts have been pursued to study various aspects associated with L-PBF of NiTi. Process optimization and parameter selection were studied in Refs. [18–21]. The effects of processing parameters on microstructure were reported in Refs. [22–25]. The phase transformation behavior of AM-fabricated NiTi was investigated in Refs. [18,22,25,26]. The relationship between processing parameters and mechanical and/or functional properties was illustrated in Refs. [23,27–32]. The influence of post-heat treatment on final parts' properties was investigated in Refs. [27,33,34]. References [13,14,35,36] provided reviews of research efforts on AM of NiTi.

One worthwhile observation upon inspecting existing literature is the fact that very few research efforts have investigated AM of NiTi

[1]Corresponding author.

Manuscript received August 10, 2021; final manuscript received June 28, 2022; published online July 29, 2022. Assoc. Editor: Ran Jin.

SMAs using a starting powder feedstock with Ni content higher than 50.8 at%, despite the fact that this is desired in order to compensate for the Ni loss during AM and realize the full application potential of final fabricated parts [19]. Indeed, the manufacturability (or printability) of high Ni content NiTi powder (Ni > 50.8 at%) is considerably more challenging compared to lower Ni contents (e.g., equiatomic composition). Xue et al. studied the printability of both $Ni_{50.1}Ti_{49.9}$ (at%) and $Ni_{50.8}Ti_{49.2}$ (at%) powder. Both powders showed good printability, with porosity associated with keyholing and lack of fusion as the main defect mode. Slight warping deformation was observed at the bottom of fabricated specimens using $Ni_{50.8}Ti_{49.2}$ (at%) powder with certain processing parameters [19]. Mahmoudi et al. investigated the printability of $Ni_{50.9}Ti_{49.1}$ (at%) powder via L-PBF and only achieved nine macroscopic defect-free samples out of 47 processing parameter combinations owing to the frequent occurrence of delamination defects [18]. With the increase of Ni content in the starting powder, warping and delamination defects become more prevalent [13]. In addition to the aforementioned defects, when the Ni composition in the starting powder is as high as 51.2 at%, elevated edge/corner or rough surfaces are observed at the early stages of the fabrication process, causing obstruction to the powder feed mechanism (counter-rotating roller or blade) and resulting in early print failure. Some of these defects are also likely to occur simultaneously. Examples of macro defects including warpage, delamination, elevated edge/corner, rough surface, and the combinations of multiple defects in L-PBF of NiTi parts using $Ni_{51.2}Ti_{48.8}$ (at%) powder feedstock are depicted in Fig. 1. Hence, limiting process optimization efforts to focus on common defects such as lack of fusion, keyholing pores, and balling are far from being sufficient. More efforts need to be spared toward eliminating other defects such as warping, delamination, elevated edge/corner, and rough surface in order to truly realize the capability of Ni-rich NiTi parts.

The importance of developing the capability to fabricate Ni-rich NiTi stems from the fact that it opens the door for truly tailoring the functional response of fabricated parts. If the transformation temperatures, shape memory, and superelastic behaviors of fabricated parts can be effectively tailored, this will greatly broaden their application prospect. For example, achieving superelasticity under body temperature for biomedical applications (e.g., stents, dental devices) requires the Ni composition in the NiTi matrix to be as high as 50.7 at% to ascertain that the austenite finish temperature is lower than body temperature [37]. Shape memory under room temperature for actuator applications (e.g., robotic arms) requires the Ni composition near equiatomic (i.e., 50.2 at%) [38].

When fabricating Ni-rich NiTi SMAs using AM, higher Ni content enables the formation of precipitates and other microstructural features by controlling the processing parameters and thermal histories during fabrication. Furthermore, since the boiling temperature of Ni (2732 °C) is lower than Ti (3287 °C), the thermal histories

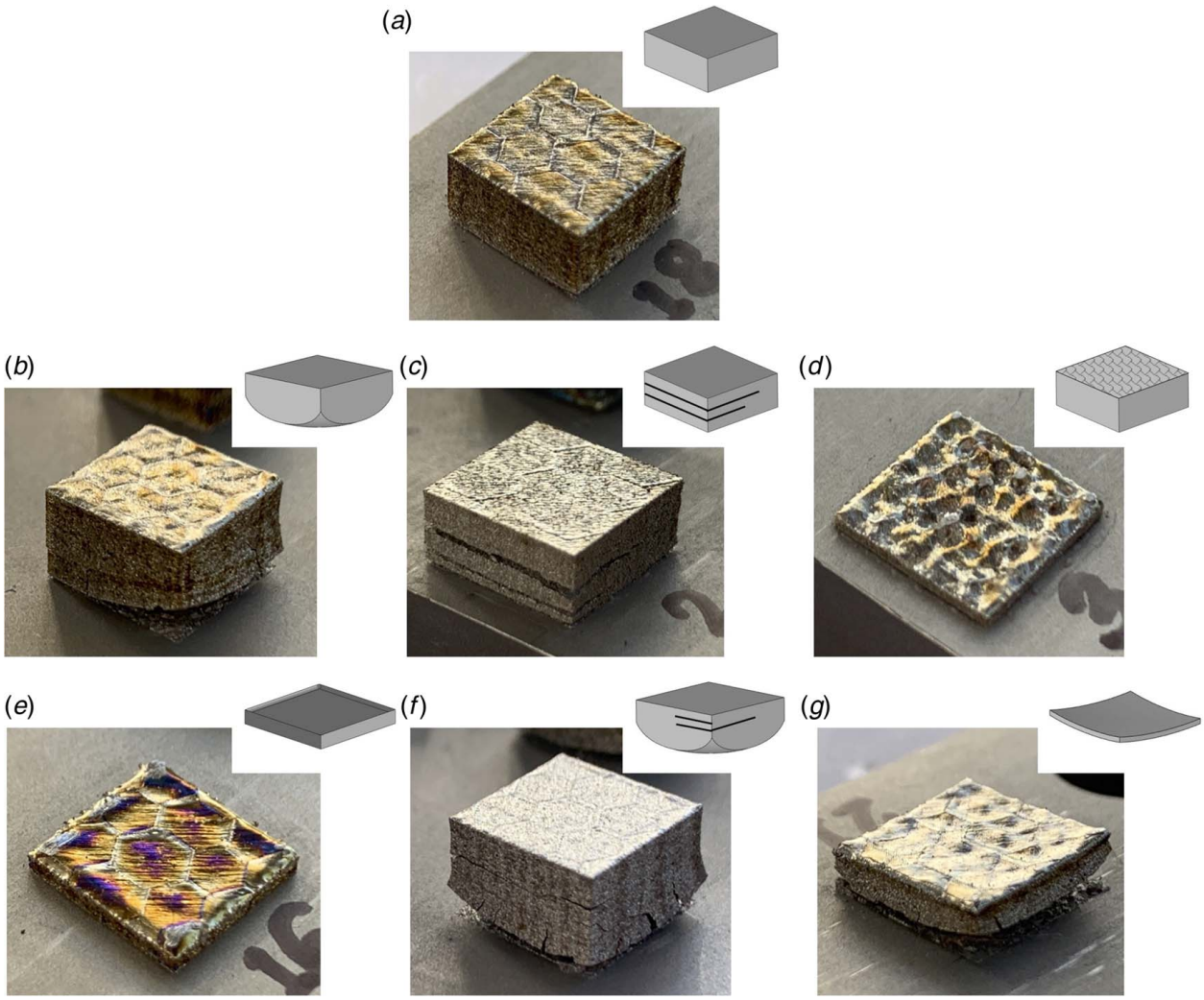

Fig. 1 Representative macroscopic defects generated during AM of NiTi cubic specimens fabricated using $Ni_{51.2}Ti_{48.8}$ (at%) powder feedstock via L-PBF: (*a*) defect-free specimen, (*b*) warping, (c) delamination, (*d*) excessively rough surface, (e) elevated edge/corner, (*f*) combination of warping and delamination, and (*g*) combination of warping and elevated edge/corner

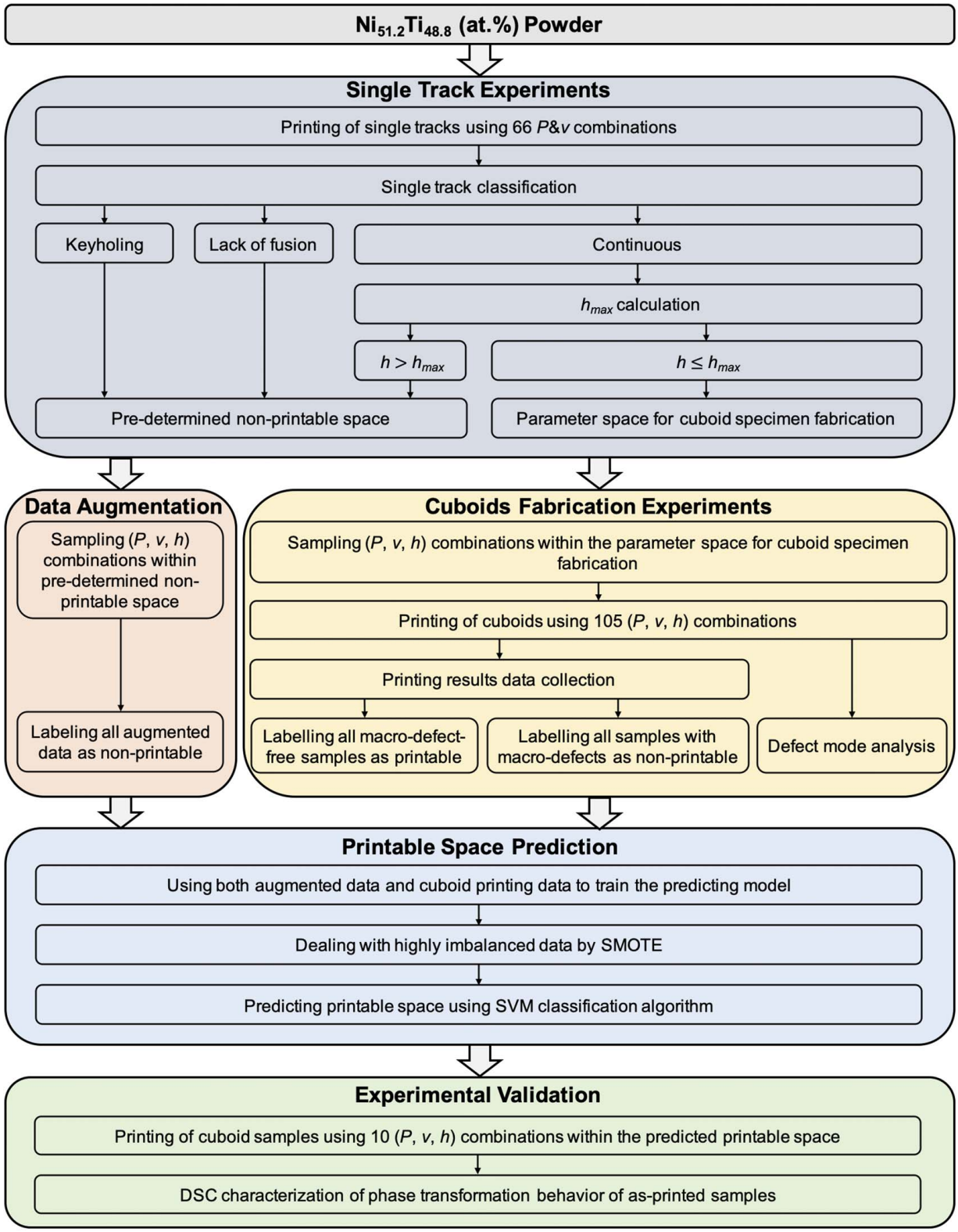

Fig. 2 Flowchart of the proposed research roadmap investigating the printability of $Ni_{51.2}Ti_{48.8}$ (at%) powder via L-PBF

can be used to control the extent of Ni differential evaporation and, in turn, vary the Ni–Ti ratio in as-printed parts. In Ni-rich compositions of NiTi, a change of 0.1 at% of Ni composition corresponds to a 10 °C change in phase transformation temperatures [37]. Hence, phase transformation, shape memory, and superelastic behaviors of as-printed parts can be effectively tuned over wide ranges, especially when the Ni content in the raw NiTi feedstock is high enough [39–43]. It has been reported in Ref. [19] that the Ni loss, depending on processing parameters, can reach up to 1% for some levels of input energy. Therefore, using a starting powder material with a Ni composition slightly higher than 51.0 at% (i.e., 51.2 at% in the current study), it can be guaranteed that the fabricated part's composition still is Ni-rich, which in turn will take full advantage of fabricated parts to meet the needs of different applications.

The current study presents a first investigation into the printability of Ni-rich $Ni_{51.2}Ti_{48.8}$ (at%) powder via L-PBF. A flowchart of the proposed research roadmap is shown in Fig. 2. Specifically, single track experiments are first conducted to classify laser power P and scanning speed v combinations that result in keyholing, lack of fusion, or continuous single tracks. The maximum hatch spacing is then calculated in accordance with the experimentally measured widths and depths of the continuous single tracks. The parameter space determined by P, v, and hatch spacing h was separated into pre-determined non-printable space and parameter space for cuboid specimen fabrication. Next, on the one hand, data augmentation was applied within pre-determined non-printable space. On the other hand, cuboid specimens are fabricated with P, v, h combinations selected within the parameter space for cuboid specimen fabrication. Since printing cuboid specimens is more challenging than printing single tracks, many of the defects and phenomena noted previously are observed and analyzed. The data collected from cuboid fabrication results, together with augmented data, were utilized to train a support vector machine (SVM) classification model in order to classify the processing parameter space (defined by P, v, and h) into printable and non-printable regions. To account for the highly imbalanced dataset—the printable region constitutes a small fraction of the total available process parameter space—the synthetic minority oversampling technique (SMOTE) method was used. Finally, 10 processing parameter combinations are selected for printing test coupons from within the predicted printable region that are applied for experimental validation, and the transformation behavior of these fabricated samples is investigated. The results of the current study could be utilized for further fine-tuning of the processing parameters inside the printable region to achieve targeted phase transformation behaviors or functional properties.

This paper is categorized as follows: Sec. 2 introduces the experimental methods utilized in this study. Results and discussion are illustrated in detail in Sec. 3. Section 4 draws conclusions and points out the future research directions.

2 Experimental Methods

2.1 Single Track Experiments. Pre-alloyed $Ni_{51.2}Ti_{48.8}$ (at%) powder prepared via gas atomization method was provided by Nanoval GmbH & Co. The 50th percentile (median) of the powder particle size distribution (D50) was 19.5 μm, while 80% of powder particles possessed a diameter less than 32 μm (D80 = 32 μm). The morphology of the NiTi powder particles is shown in Fig. 3, captured using an FEI Quanta 600 field emission gun (FEG) scanning electron microscope (SEM). Most powder particles show spherical morphology, although some hollow, satellite, and irregularly shaped particles are also visible. It is worth mentioning that the powder particle morphology would also affect the printability and final part properties, while it is not the focus of the current study. The interested reader is directed to Ref. [13] for more details.

About 66 single tracks with a length of 10 mm were printed on a sand-blasted NiTi disk (for better powder coverage) using a ProX 200 DMP commercial L-PBF system from 3D Systems (with a maximum laser power of 260 W and a laser spot size of 80 μm) using different P and v combinations (Fig. 4). The gray dashed lines shown in Fig. 4 represent the boundaries of the processing parameter window investigated in this study. The upper limits of P (260 W) and v (2.5 m/s) were defined by the machine specifications. The lower limit of v was set as 0.05 m/s to mimic the steady yet moving laser status. The lower limit of P was set as 21 W, which was the minimum laser power required to obtain the maximum temperature of the melt pool higher than the melting temperature of $Ni_{51.2}Ti_{48.8}$ (at%) at the lower limit of v, derived using the Eagar–Tsai analytical model [44]. Among these 66 combinations, 60 were chosen using grid sampling with P varying between 40 W and 240 W with an increment of 40 W, and v varying between 0.08 m/s and 2.33 m/s with an increment of 0.25 m/s. To better quantify the region of low P and low v combinations, six additional single tracks were sampled at P of 60 W, 100 W, and 140 W with v of 0.205 m/s and 0.405 m/s. These additional points are important because this region has a more localized change with the change of P and/or v in terms of single track morphologies [45]. The layer thickness was chosen as the D80 of the powder size distribution (32 μm). After single track experiments, the top surfaces of single tracks were investigated under SEM to identify whether a lack of fusion happened and to measure the melt pool widths. A relatively conservative lack of fusion criterion was utilized in this study according to whether the single track was continuous or not. A discontinuous single track indicated that the energy density applied to the powder bed could not penetrate the powder layer, which would result in porosity due to lack of fusion. The linear energy density E_L is defined as P/v, which is a simplified aggregate design parameter quantifying the amount of laser energy delivered per unit length to the powder bed. The single track width (w) was calculated as the average of single track widths measured at five locations.

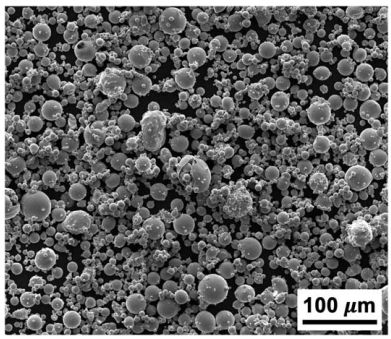

Fig. 3 Morphology of the $Ni_{51.2}Ti_{48.8}$ (at%) powder utilized in this study captured using SEM. The majority of the powder particles are spherical, while some hollow, satellite, and irregular-shaped particles also exist.

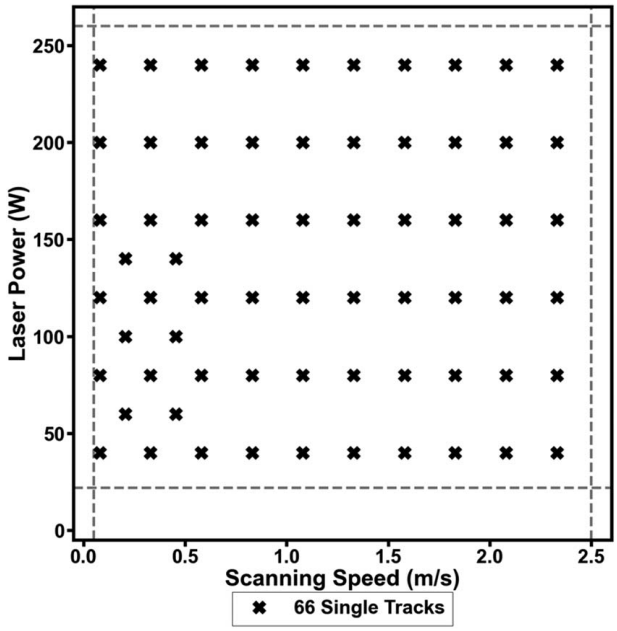

Fig. 4 Laser power P and scanning speed v combinations selected for single track experiments. The gray dashed lines represent the boundaries of the processing parameter window investigated in this study.

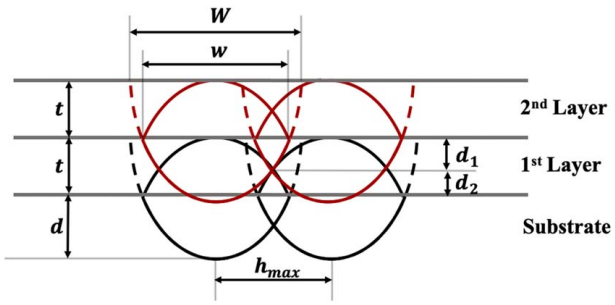

Fig. 5 Graphical representation of the geometric relationships under maximum hatch spacing h_{max}. Black dashed lines represent the melt pools generated during the first layer melting; black solid lines represent the geometry of solid tracks after the first layer solidification; dashed lines and solid lines represent the melt pools and solid tracks generated during the second layer melting, respectively. h_{max} represents the maximum hatch spacing, d represents the measured depth of the melted track, w represents the measured width of the melted track, W represents the width of the melt pool, and t represents the layer thickness.

The single tracks were subsequently cross-sectioned at three equidistant locations using wire electrical discharge machining (EDM) to detect whether the keyholing phenomenon happened and to measure the track depths. The cross-sections were ground by SiC paper up to 1200 grit and polished by water-based diamond suspension and characterized under Keyence VHX digital optical microscope (OM). The single track depth (d) was calculated as the average of single track depths measured at these three locations. A single track was defined as keyholing if 1.2 times single track depth was greater than the single track width ($d > w/1.2$). A single track with a keyholing defect would exhibit keyhole porosity, which is detrimental to the quality of the fabricated parts. The processing parameter combinations of P and v which resulted in a lack of fusion or keyholing defects were excluded for the next step involving the fabrication of cuboid specimens.

It is worth noting that balling is also a common phenomenon during the L-PBF process, which exhibits a non-uniform ellipsoidal/spherical agglomeration or humping and is caused by the Plateau–Raleigh capillary instability at high laser power and high scanning speed combinations [46]. When the balling phenomenon is excessive, irregular broken tracks would be noticed. The balling phenomenon is closely related to the material properties and processing parameters [47]. In this study, the excessive balling phenomenon was not observed, with all single tracks exhibiting balling phenomenon still being continuous. Therefore, the corresponding processing parameter was considered a candidate for cuboid specimen fabrication as long as the balling single track was continuous.

2.2 Cuboid Specimens Fabrication. Cuboid specimens with sizes 10 mm × 10 mm × 5 mm were attempted to be fabricated using the P and v combinations that resulted in continuous single tracks. The maximum hatch spacing h_{max} for each P, v combination was calculated based on the geometric relationships between single track depth d, width w, and h_{max} in order to achieve full fusion within and across powder layers. Specifically, as shown in Fig. 5, assuming that the cross-sectional geometry of the melt pool takes a parabolic shape, the following relationships exist when the hatch spacing is equivalent to h_{max}:

$$d = A \times \left(\frac{w}{2}\right)^2 \tag{1}$$

$$d_1 = d - A \times \left(\frac{h_{max}}{2}\right)^2 \tag{2}$$

$$\frac{d_1}{d} = \frac{d_2}{t} \tag{3}$$

$$d_1 + d_2 = t \tag{4}$$

The parabolic melt pool shape was assumed considering previous studies indicated that the melt pool shape could be fit by a parabolic curve when the L-PBF process is operating in the conduction mode [48–50]. From Eq. (1), $A = 4d/w^2$. Substituting A into Eq. (2), $d_1 = d\left(1 - \frac{h_{max}^2}{w^2}\right)$. Combining Eqs. (3) and (4), $d_1 = (t \times d/t + d)$. Therefore, h_{max} could be computed as

$$h_{max} = w \times \sqrt{\frac{d}{d+t}} \tag{5}$$

The hatch spacing values for cuboid specimens under each P and v combination were selected from the range between 25 μm and the computed maximum hatch spacing h_{max}. Selecting 25 μm as the lower bound of the hatch spacing value is justified as follows: first, it guarantees that at least one hatch spacing value could be selected for each P, v combination since the calculated h_{max} for each P, v combination selected for cuboid specimen fabrication was higher than or equal to 25 μm. Second, considering the fact that lowering hatch spacing would increase the total fabrication time, 25 μm is a reasonable lower bound value for hatch spacing in terms of balancing process efficiency. In total, 105 processing parameter combinations with different P, v, and hatch spacing h values were selected for cuboid specimen fabrication. All samples were fabricated under an argon protective atmosphere with oxygen levels controlled under 100 ppm to minimize oxidation. The laser scanning strategy utilized for cuboid specimen fabrication was the hexagonal scanning strategy with a hexagon edge size of 2 mm ($R = 2$ mm) and overlap between two adjacent hexagons of 200 μm ($O = 200$ μm) (Fig. 6(*b*)). Inside each hexagon, the laser scanning angle was set as 45 deg for the first layer in back and forth style and was rotated 90 deg from layer to layer (Fig. 6(*a*)). The hexagon location was modified from one layer to the other to mitigate the porosity associated with constant overlap zones [51]. Specifically, the center of each hexagon in layer n would become the vertex in layer $n + 1$. The justification for using the hexagonal scanning strategy is to reduce residual stresses via reduced scanning length. Promoppatum and Yao [52] demonstrated that the residual stress could be reduced by 50% by applying reduced

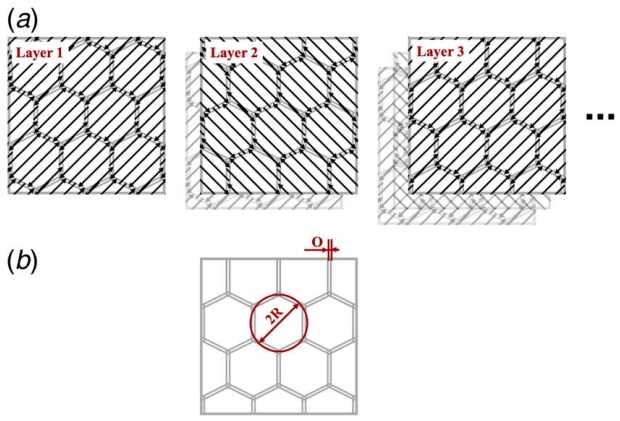

Fig. 6 Schematic of the hexagonal scanning strategy utilized in cuboid specimen fabrication: (*a*) the laser scanning direction and the hexagonal segmentation for each layer and (*b*) the representation of the hexagon size and overlap between two adjacent hexagons

scanning length. All NiTi cuboid specimens were printed on NiTi substrates to eliminate the potential lack of compatibility effect between the melted material and the base substrate [53]. The fabrication outcomes for these specimens were classified and labeled as printable or non-printable. For the non-printable specimens, the corresponding macro defects were also labeled for further analysis.

2.3 Prediction of the Printable Space. SVM was utilized to predict the printable region within the P, v, and h space. SVM is a widely used classification algorithm identifying the maximum-margin hyperplane that best classifies the observations into two classes [54]. Benefiting from the implementations of kernel trick and soft margin, SVM is effective for linearly non-separable classification problems. Formally, the SVM classifier could be obtained by computing Eq. (6) [55]

$$\max_{f(\alpha_1,\ldots,\alpha_N)} \left\{ \sum_{i=1}^{N} \alpha_i - \frac{1}{2} \sum_{i=1}^{N} \sum_{j=1}^{N} \alpha_i \alpha_j y_i y_j K(\boldsymbol{x}_i, \boldsymbol{x}_j) \right\} \tag{6}$$

subject to $\sum_{i=1}^{N} \alpha_i y_i = 0$ and $0 \le C$ for $i = 1, \ldots, N$. α_i defines whether the ith observation is the support vector. C is the soft margin parameter which quantifies the margin size. N is the number of training samples. $\boldsymbol{x}_i$ represents the ith predictor with dimension p. In this study, $p = 3$ (P, v, and h). y_i is the ith response variable taking values from $\{-1, +1\}$, in which -1 stands for non-printable and $+1$ stands for printable. $K(\cdot, \cdot)$ is the kernel function that transforms predictor space into higher dimensions. The radial-basis function (RBF) shown in Eq. (7) was selected as the kernel utilized in this study due to its ability of taking local behavior into account [56], where γ quantifies the similarity of two predictor points at a given Euclidean distance. The hyperparameters C and γ were selected by grid searching on $C \in \{10^{-1}, \ldots, 10^{7}\}$, $\gamma \in \{10^{-3}, \ldots, 10^{1}\}$, and the combination which resulted in the highest accuracy after 5-fold cross-validation was selected. $\in$

$$K(\boldsymbol{x}_i, \boldsymbol{x}_j) = \exp\left(-\gamma \sum_{k=1}^{p} (x_{ik} - x_{jk})^2 \right) \tag{7}$$

The dataset utilized to train the SVM model was comprised of three parts. The first part was the data points collected from the cuboid specimen fabrication results (Sec. 2.2). The second part was obtained through augmentation of P and v combinations which resulted in a lack of fusion or keyholing defects during single track experiments. In particular, the data augmentation method was utilized through sampling a series of hatch spacing values for each P and v combination. The third part was obtained by sampling at the high hatch spacing region ($h > h_{\max}$) for P and v combinations associated with continuous single tracks. It is worth mentioning that all the augmented data were labeled as non-printable since porosity defect would occur if these processing parameter combinations were applied for solid part fabrication. Figure 7 shows an example of how data augmentation works at $P = 160$ W, in which dot markers indicate printable ($y = +1$) and cross markers indicate non-printable ($y = -1$). The black dots and crosses represent the cuboid specimen fabrication results. The crosses are the augmented training data sampled in the lack of fusion or keyholing region with h sampled in $H = \{10, 25, 50, 100, 150, 200\ \mu\text{m}\}$ to sweep over the whole hatch spacing range. The blue crosses are the augmented training data sampled in the high hatch spacing region with h sampled from $\{h: (h > h_{\max}) \cap (h \in H)\}$. The purpose of data augmentation is to incorporate more information of what gained in Secs. 2.1 and 2.2 to train the SVM model. Otherwise, the model itself would not know that the lack of fusion region, keyholing region, and the high hatch spacing region are non-printable.

After data augmentation, the final dataset contained 401 observations in total, only 29 of which were labeled as printable. Therefore, the dataset was skewed to the non-printable class with

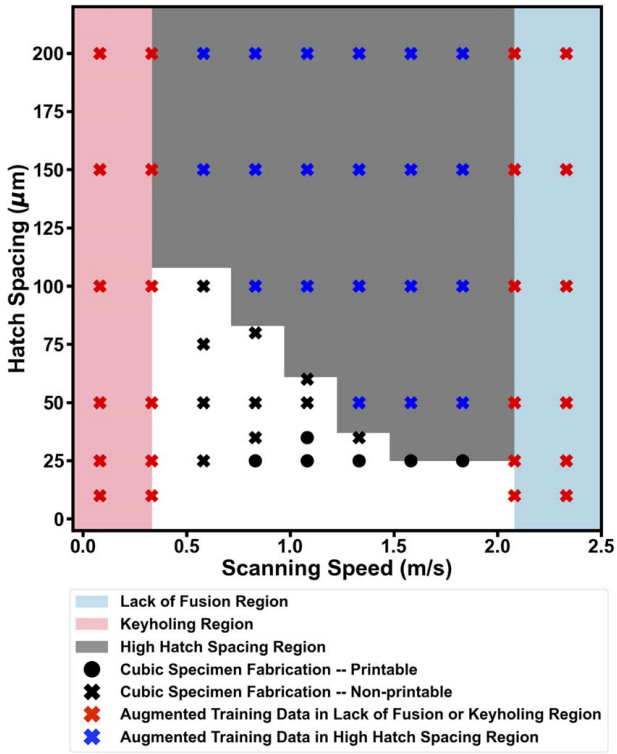

Fig. 7 Example of the augmented dataset utilized to train the SVM model at laser power $P = 160$ W. Left shaded area represents the keyholing region; right shaded area represents the lack of fusion region; upper middle shaded area represents the high hatch spacing region where $h > h_{\max}$; dots stand for the printable processing parameters gained from cuboid specimen fabrication; crosses within the lower middle blank area stand for non-printable processing parameters obtained by cuboid specimen fabrication, in which non-printable indicates when macro defect is detected; crosses within both the left and right shaded area are the augmented data in lack of fusion and keyholing regions; crosses within the upper middle shaded area are the augmented data in the high hatch spacing region.

majority-to-minority class ratio higher than 12—in other words, the dataset was heavily imbalanced. To account for this imbalance, synthetic minority oversampling technique (SMOTE) was utilized to synthesize new data points labeled as printable and achieve a balanced distribution with equal amount of data points in printable and non-printable classes. Details of SMOTE method could be found in Ref. [57]. In simple terms, the new data points in the minority class were randomly sampled on a line connecting two adjacent minority data points. It is worth mentioning that during the 5-fold cross-validation mentioned earlier to select the best hyperparameters, for each iteration, SMOTE was only implemented on the subsets used as the training set in which a balanced dataset is desired, while the holdout fold used as the test set was kept as is to ascertain the accuracy of cross-validation. Finally, the cross-validation selected hyperparameters were utilized to train the SVM model on the full dataset oversampled by SMOTE and the resulting predictive printability map was constructed within the P, v, and h space. To validate the printable region predicted by SVM, 10 processing parameter combinations were chosen within the predicted printable region and the 10 mm × 10 mm × 10 mm cubic samples were test fabricated using these processing parameter combinations. Differential scanning calorimetry (DSC, TA Instruments Q2000) was utilized to measure the phase transformation behavior of these test samples. Cuboid DSC specimens with dimensions 3 mm × 3 mm × 1 mm were cut from the middle part of these cubic samples by wire EDM. Two heating/cooling cycles from 150 °C to −150 °C with a temperature changing rate of 10 °C/min were applied.

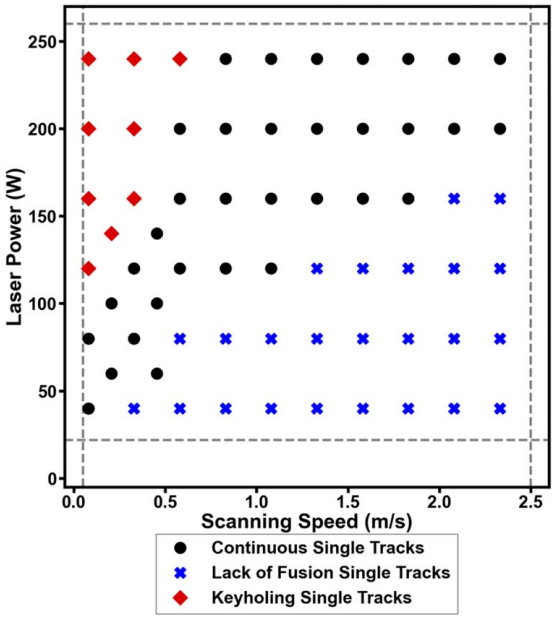

Fig. 8 Experimentally classified continuous, keyholing, and lack of fusion single tracks overlaid onto the processing parameter space defined by laser power and scanning speed. The crosses, diamonds, and dots stand for lack of fusion, keyholing, and continuous single tracks, respectively. The dashed lines represent the boundaries of processing parameters investigated in this study.

Table 1 Maximum hatch spacing h_{max} for laser power P, scanning speed v combinations resulting in continuous single tracks

Track #	Laser power P (W)	Scanning speed v (m/s)	E_L (J/m)	Layer thickness t (μm)	h_{max} (μm)
1	40	0.080	500	32	100
2	60	0.205	293	32	87
3	60	0.455	132	32	29
4	80	0.080	1000	32	189
5	80	0.330	242	32	83
6	100	0.205	488	32	150
7	100	0.455	220	32	89
8	120	0.330	364	32	122
9	120	0.580	207	32	92
10	120	0.830	145	32	59
11	120	1.080	111	32	35
12	140	0.455	308	32	111
13	160	0.580	276	32	108
14	160	0.830	193	32	83
15	160	1.080	148	32	61
16	160	1.330	120	32	37
17	160	1.580	101	32	25
18	160	1.830	87	32	25
19	200	0.580	345	32	118
20	200	0.830	241	32	99
21	200	1.080	185	32	82
22	200	1.330	150	32	66
23	200	1.580	127	32	54
24	200	1.830	109	32	51
25	200	2.080	96	32	25
26	200	2.330	86	32	25
27	240	0.830	289	32	118
28	240	1.080	222	32	99
29	240	1.330	180	32	84
30	240	1.580	152	32	73
31	240	1.830	131	32	69
32	240	2.080	115	32	42
33	240	2.330	103	32	40

3 Results and Discussion

3.1 Single Track Experimental Results. The results of single track experiments are shown in Fig. 8. Different colors correspond to different classes of single tracks. The processing parameter combinations resulting in keyholing single tracks are shown as diamonds and representative top-view SEM image and corresponding cross-sectional OM image are shown in Fig. 9(*a*). The gas pore shown in the cross-sectional OM image was caused by the evaporation of melted material due to the high energy input applied to the powder bed and subsequent collapse of the vapor cavity [58]. Keyholing porosity is detrimental to the fabricated part's properties. The processing parameter combinations resulting in a lack of fusion single tracks are shown as blue crosses in Fig. 8. Almost no track or a highly discontinuous track are classic forms of this class. Figure 9(*d*) shows the representative top and cross-section of a lack of fusion single track. The processing parameter combinations utilized in the lack of fusion tracks did not cause sufficient penetration and melting of the powder layer and bonding between deposition material and substrate. This ultimately resulted in a lack of fusion porosity which also compromised the fabricated part's properties. The processing parameter combinations resulting in continuous single tracks are shown as black dots in Fig. 8. Two classes of single tracks were considered as continuous: good single tracks (Fig. 9(*b*)), which were uniform and continuous, and balling single tracks (Fig. 9(*c*)), which were non-uniform but continuous. The balling phenomenon would affect the surface roughness of printed samples [59]. However, in virtue of its continuity, it was still possible to use these processing parameter combinations to produce defect-free part if the hatch spacing was tuned to a smaller value. Therefore, the processing parameter combinations

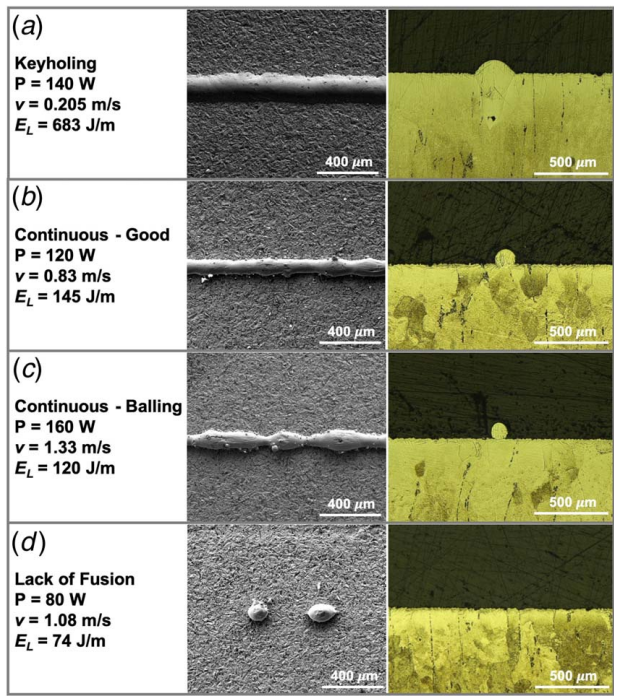

Fig. 9 Representative top view (*a*) SEM and (*b*) cross-sectional OM images of single tracks for different laser power P and scanning speed v combinations showing different track classifications: (*a*) Keyholing single track. Bell-shaped melt pool is shown in the OM image. Keyholing pore is noticed at the bottom of the melt pool, (*b*) good single track. Uniform and continuous track morphology is obtained, (*c*) balling single track. Although some humping phenomenon exists, the track is still continuous, and (*d*) lack of fusion track. The applied energy could not penetrate the powder layer, causing a discontinuous single track.

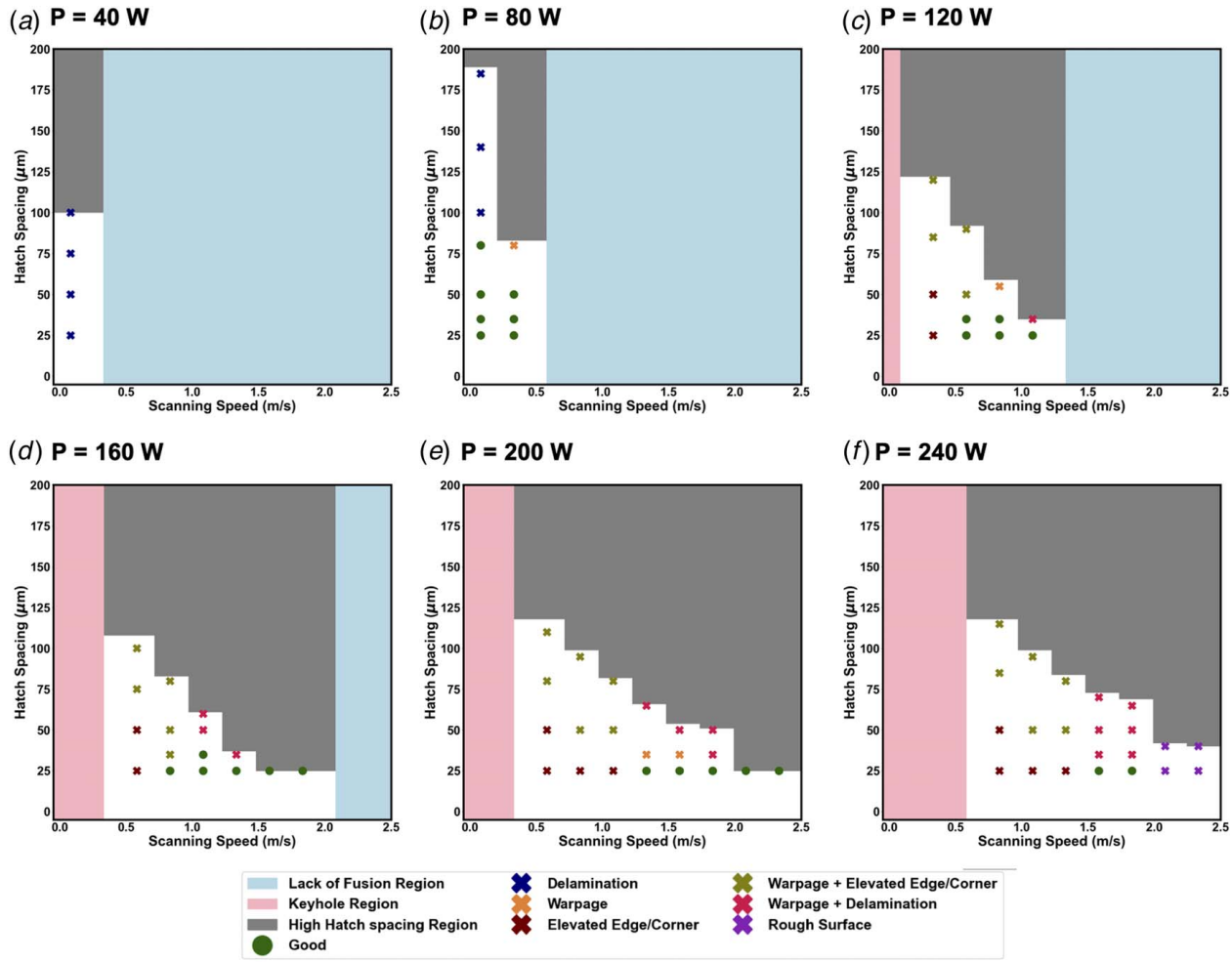

Fig. 10 Cuboid specimen fabrication results overlapped on the laser scanning speed and hatch spacing map at: (*a*) $P = 40$ W, (*b*) $P = 80$ W, (*c*) $P = 120$ W, (*d*) $P = 160$ W, (*e*) $P = 200$ W and (*f*) $P = 240$ W. Dots stand for processing parameters resulting in macro defect-free cuboid specimen; crosses stand for processing parameters leading to macro defects in fabricated cuboid specimens with different macro defect modes.

resulting in both good and balling tracks were considered continuous and chosen for cuboid specimens fabrication.

3.2 Cuboid Specimens Fabrication Results. The P and v combinations that resulted in continuous single tracks were selected to print the cuboid specimens using a series of hatch spacing values. The maximum hatch spacing values for P and v combinations resulting in continuous single tracks were calculated and are shown in Table 1. The hatch spacing values chosen for cuboid specimens fabrication are located in the range below the maximum hatch spacing values as illustrated in Sec. 2.2. In total, 105 processing parameter combinations of P, v, and h were selected for cuboid specimen fabrication. All other processing parameters were kept constant throughout the fabrication process. There were six macro-defect modes observed (Fig. 1), and the corresponding processing parameters at six different laser power levels are shown in Fig. 10, in which green dots represent printable processing parameters, and all crosses represent processing parameters resulting in macro-defects. Details regarding each mode are summarized as follows:

(1) *Warpage*: Warpage was the distortion phenomenon that happened during L-PBF where the bottom portion of the specimen was tilted (or warped) due to the accumulation and relief of thermal-induced residual stress [60], as shown in Fig. 1(*b*). Compared to the geometry of the defect-free specimen (Fig. 1(*a*)), the contact area between the warping specimen and the substrate was reduced, causing it to be easily removed by the powder feed roller, which resulted in build failure. The processing parameters resulting in warpage defect are shown as orange crosses in Figs. 10(*b*), 10(*c*) and 10(*e*). It could be noticed that individual warpage defect was rarely observed and at slightly higher hatch spacing values compared with the printable processing parameters with the same P and v combinations. For example, when hatch spacing increased from 50 μm to 75 μm at a fixed laser power of 80 W and scanning speed of 0.33 m/s, a noticeable warpage defect would occur. This aligns well with the results derived in Ref. [61]. At lower hatch spacing values, the amount of material subject to reheating/remelting increased with the increase in the overlap between adjacent tracks, which provided an annealing effect to reduce the residual stress and in return mitigate the warpage.

(2) *Delamination*: Delamination was a macro defect that was also caused by the relief of accumulated residual stress generated during the fabrication process [62]. Unlike warpage defect, delamination was manifested as the interlayer cracks perpendicular to the building direction, as depicted in Fig. 1(*c*), which was caused due to the low tensile strength

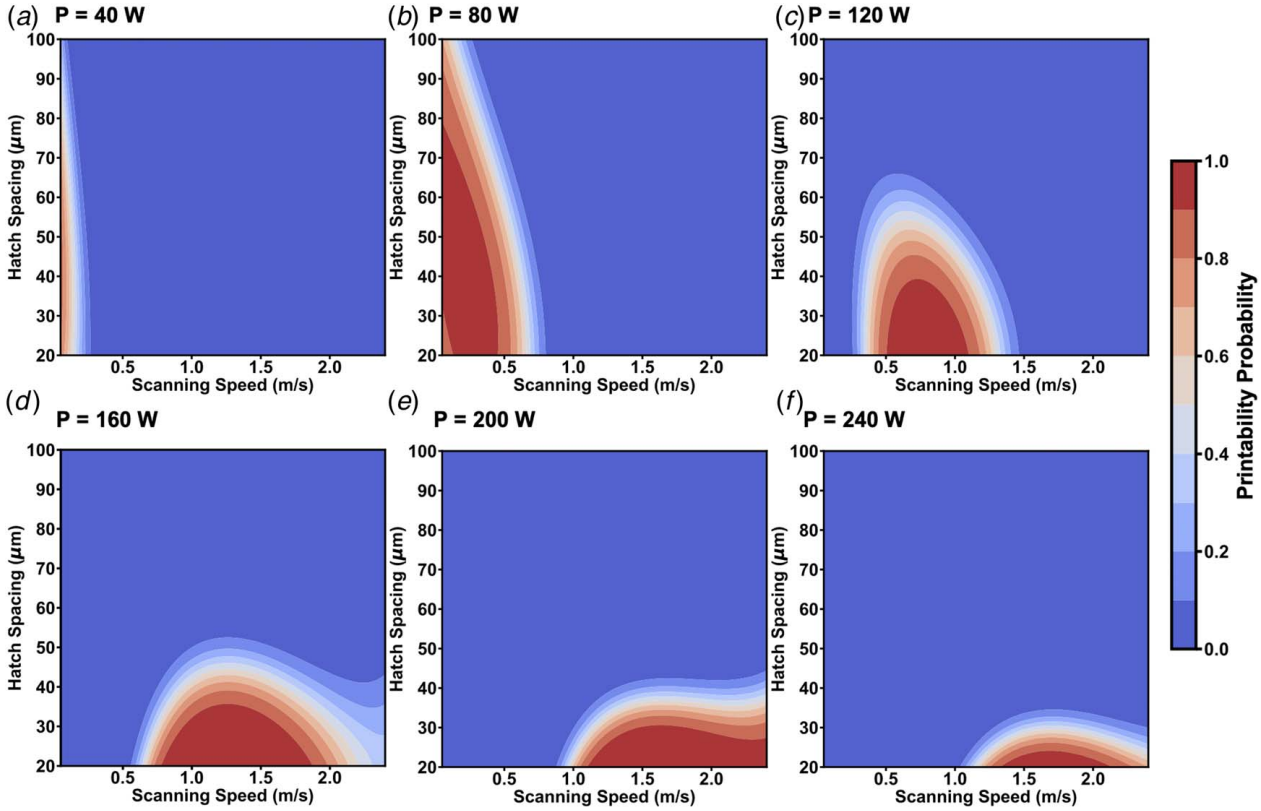

Fig. 11 The predicted printable region via SVM classification at: (*a*) $P = 40$ W, (*b*) $P = 80$ W, (*c*) $P = 120$ W, (*d*) $P = 160$ W, (*e*) $P = 200$ W and (*f*) $P = 240$ W. The colorbar represents the probability of a successful print between 0 and 1.

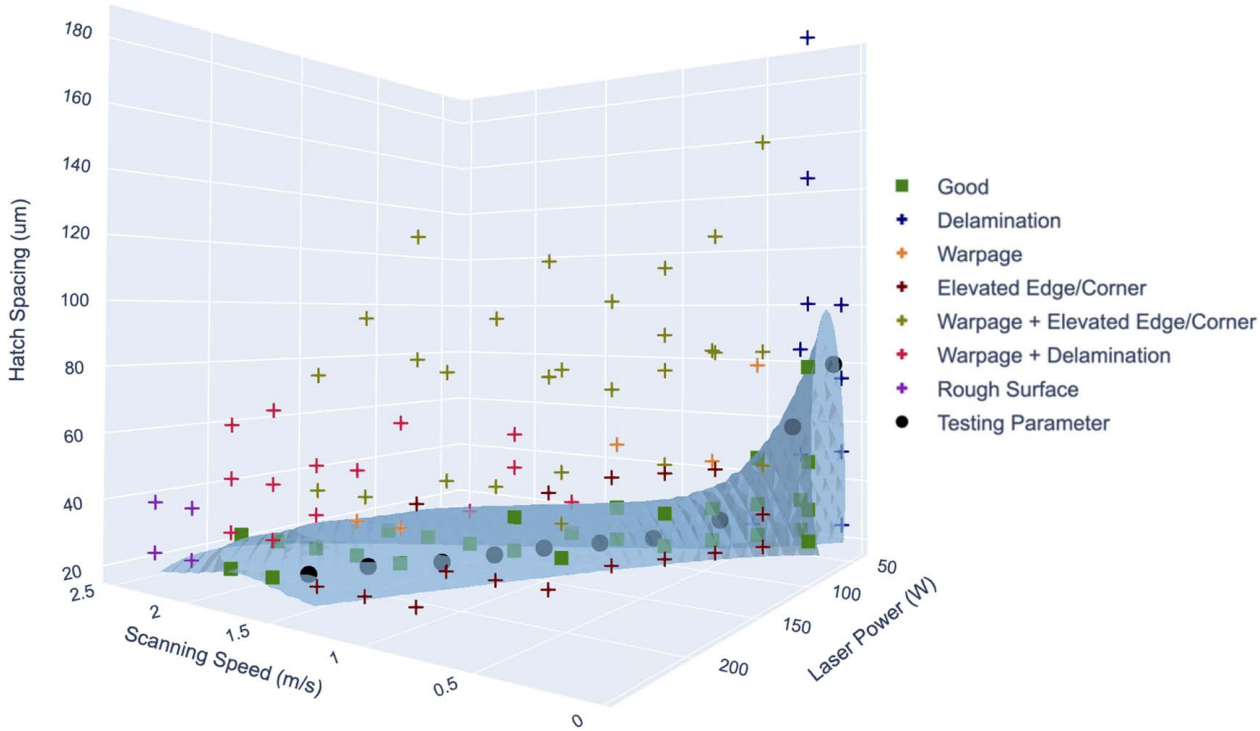

Fig. 12 The predicted printable 3D space defined by laser power *P*, scanning speed *v*, and hatch spacing *h*. The space below the blue surface is predicted as printable.

Table 2 The processing parameters applied for test prints

Test print #	P (W)	v (m/s)	h (μm)	t (μm)	E_L (J/m)	E_V (J/mm^3)
Test 1	50	0.08	80	32	625	244
Test 2	70	0.20	60	32	350	182
Test 3	90	0.47	30	32	191	199
Test 4	110	0.70	25	32	157	196
Test 5	130	0.85	25	32	153	191
Test 6	150	1.00	25	32	150	188
Test 7	170	1.10	25	32	155	193
Test 8	190	1.20	25	32	158	198
Test 9	210	1.40	25	32	150	188
Test 10	230	1.50	25	32	153	192

along the building direction resulting from the incomplete fusion and adhesion between successive layers. The processing parameters resulting in delamination are shown as blue crosses in Figs. 10(*a*) and 10(*b*). Individual delamination defect was inclined to generate at lower laser power ($P =$ 40, 80 W) and higher hatch spacing ($h \geq 100$ μm for $P =$ 80 W and $v = 0.08$ m/s), within which region E_V was relatively low.

(3) *Rough surface*: Bumpy top surfaces were detected (Fig. 1(*d*)) at high laser power ($P = 240$ W) and high scanning speed ($v \geq 2.08$ m/s) scenarios, shown as purple crosses in Fig. 10(*f*). The peaks of these bumpy surfaces could project from the powder bed and cause collision with the movement of the powder feeding mechanism. Furthermore, the rough surface would cause the non-uniform powder spreading and in turn degrade the fabricated part properties. This defect type was caused due to the combined action of surface tension and flow inertia, which promoted swelling formation at the end of the melt pool [63].

(4) *Elevated edge/corner*: The elevated edge/corner phenomenon during the L-PBF process (Fig. 1(*e*)), also called the edge/corner effect, was caused by the heat accumulation near the edge/corner of the printing area, where the surrounding powder bed possessing low thermal conductivity slowed the thermal dissipation process [64,65]. Similar to the rough surface defect, the elevated edge/corner was harmful to the printability of $Ni_{51.2}Ti_{48.8}$ (at%) powder investigated in the current study given that it collides with the powder recoating roller as it deposits powder for the next layer. This generates a significant torque that could stop the movement of the recoating system and consequently stop the fabrication process. The elevated edge/corner defect often happened at an early stage and specimens with such defect often failed at a very early age. The processing parameters leading to elevated edge/corner are represented as rufous crosses in Figs. 10(*c*)–10(*f*). It could be noticed that this defect form was associated with lower scanning speed values at higher laser power ($P \geq 120$ W), in which higher thermal accumulation was generated due to higher E_L.

(5) *Combined warpage + delamination*: In addition to the aforementioned four distinctive defects, certain processing parameters led to more than one macro defect. The combination of warpage and delamination is illustrated in Fig. 1(*f*), and the corresponding processing parameters are marked as rose-crosses in Figs. 10(*c*)–10(*f*). Similar to individual warpage defects, the hatch spacing resulting in this defect mode was relatively higher than the printable points with the same P and v combinations. Higher hatch spacing is associated with lower E_V, which facilitated the generation of delamination defect.

(6) *Warpage + elevated edge/corner*: Figure 1(*g*) represents the typical profile of this defect mode. The specimen with such combinations of defects would fail at a premature age since the powder feeding mechanism would easily peel it off from the substrate. The processing parameters generating such defects are shown as olive crosses in Figs. 10(*c*)–10(*f*). All crosses were located at higher hatch spacing and lower scanning speed region, which aligned well with the locations for individual warpage and individual elevated edge/corner defects as discussed before.

3.3 Machine Learning Classification Results. SVM was utilized to classify the processing parameter space of P, v, and h into printable and non-printable regions as described in Sec. 2.3. The final SVM model with hyperparameters tuned using 5-fold cross-validation possessed the RBF kernel with $\gamma = 10^{-1}$ and $C = 10^7$. This hyperparameter combination resulted in an accuracy of 0.988 in the cross-validation step.

Figure 11 shows the classification results at six different values of laser power P, with horizontal and vertical axes representing scanning speed v and hatch spacing h, respectively. In the circumstance when P was too low ($P = 40$ W), no printable processing parameter was detected as shown in Fig. 11(*a*). When P was reasonably low ($P = 80$ W), the printable hatch spacing range was comparatively

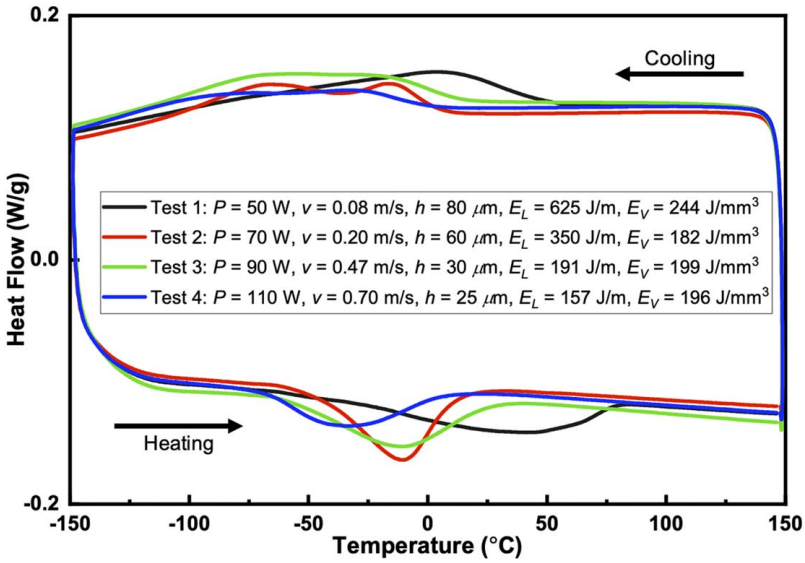

Fig. 13 DSC results showing the transformation behavior of four printed test specimens

wider (Fig. 11(*b*)). With the increase of P, the printable values of v increased while the printable hatch spacing was narrowed to lower values. The occurrence of rough surface defect at $P = 240$ W further narrowed the printable region. This pattern could be explained by macro defect modes. In the lower power situation ($P \leq 80$ W), the major defect mode was delamination. With the increase of P ($P \geq 120$ W), multiple defects were generated at different v and h combinations, which significantly narrowed the printable region.

The 3D representation of the predicted printable region is shown in Fig. 12. The blue surface represents the iso-probability contour plane with a printable probability of 0.9. Below that surface, the printable probability is higher than 0.9 and the corresponding processing parameters were considered printable. The green squares and crosses with different colors indicate the printable processing parameters and parameters leading to macro defects resulting from cuboid specimen fabrication, respectively. For detailed information on the processing parameters and corresponding fabrication results and/or defect modes, please refer to Table 3 in Appendix. It could be seen that SVM classification results performed well in splitting the printable processing parameters from non-printable parameters. With the laser power P ranging from 50 W to 100 W, the printable region narrowed down drastically with feasible hatch spacing value decreasing from 80 to 40 μm. With further increase of the laser power, the printable region was found to be confined to a narrow "tube," with a hatch spacing value of less than 30 μm. This was in accordance with what was detected in Fig. 11.

3.4 Validation of Machine Learning Classification Model. Ten processing parameter combinations inside the predicted printable region were selected and test fabricated to validate the proposed classification model. The points are shown as black dots in Fig. 12. The detailed processing parameters are listed in Table 2. All ten samples were built successfully, free of macroscopic defects. Figure 13 shows the transformation behavior (obtained by DSC characterization) of four representative as-fabricated samples, showing an increasing trend in transformation temperature with increasing linear energy density E_L. At a smaller P value ($P = 50$ W), a high E_L value could be successfully applied, which resulted in higher Ni evaporation and in turn led to higher transformation temperatures. With the increase of P, the printable E_L gradually decreased and the transformation temperatures were consequently reduced. When P exceeded 100 W, the transformation behavior didn't show a noticeable difference due to the relatively constant E_L and E_V settings. It could be seen that although the printable region for $Ni_{51.2}Ti_{48.8}$ (at%) was quite narrow compared with relatively lower Ni compositions investigated in previous studies [18,19], the range over which transformation temperatures can be tuned was still larger than NiTi compositions with lower Ni content [18]. This demonstrates the potential of Ni-rich NiTi compositions in tailoring transformation temperatures and further emphasizes the impact of the current study.

4 Conclusions and Future Work

4.1 Conclusions. In the current study, the printability of high Ni-content $Ni_{51.2}Ti_{48.8}$ (at%) powder via L-PBF was investigated. A variety of macro defect modes were detected during the fabrication process. The cause of these defects was systematically investigated, and the relationship with key processing parameters was analyzed. The printable region within the space defined by laser power P, scanning speed v, and hatch spacing h was predicted via the SVM classification model and validated by test printing. The conclusions are summarized as follows:

(1) Compared to NiTi powder feedstock with lower Ni compositions investigated in previous studies, the printability of $Ni_{51.2}Ti_{48.8}$ (at%) is significantly degraded and the printable region within the 3D space defined by laser power P, scanning speed v, and hatch spacing h is narrowed. These processing parameter combinations should be fine-tuned in order to achieve parts free of macropscopic defects.
(2) In addition to the lack of fusion and keyholing defects, several different types of macroscopic defects, namely delamination, warpage, rough surface, and elevated edge/corner were observed during the fabrication process which highly compromised the printability of $Ni_{51.2}Ti_{48.8}$ (at%) powder. The combination of more than one defect (warpage + delamination, warpage + elevated edge/corner) also emerged. Elevated edge/corner defect was associated with a lower scanning speed at higher laser power ($P \geq 120$ W). Warpage happened along with relatively higher hatch spacing values. Delamination defect was generated when the energy input was relatively low. Rough surface was caused by the combination of high laser power ($P = 240$ W) and high scanning speed ($v \geq 2.08$ m/s). The occurrence of more than one defect was detected when the processing parameters that favored the generation of multiple defects were chosen.
(3) At lower laser power ($P < 100$ W) settings, the printable region was relatively large. On the contrary, at higher laser power ($P \geq 100$ W) settings, the printable region was narrowed to a low hatch spacing range.
(4) The transformation behavior of as-printed samples showed a clear trend relative to linear energy density. In order to achieve higher transformation temperatures, a lower P value ($P < 100$ W) should be considered due to the higher likelihood of successful prints at lower scanning speed.

4.2 Future Work. Since the functional properties of NiTi SMAs, e.g., SME and SE, are the most attractive properties of this class of alloys, the relationships between processing parameters and the transformation temperatures as well as these functional properties for NiTi specimens fabricated via L-PBF will be studied systematically in future work. The effects of other processing parameters, e.g., scanning strategy, and post-heat treatment will also be studied in detail in future work.

Acknowledgment

The co-authors thank the support from NSF through Grant No. 1846676.

Data Availability Statement

The datasets generated and supporting the findings of this article are obtainable from the corresponding author upon reasonable request.

Appendix

Table 3 Cuboid specimen fabrication results

Cuboid specimen #	P (W)	v (mm/s)	h (μm)	E_L (J/m)	E_V (J/mm^3)	h_{max} (μm)	Defect mode
1	40	80	25	500	625	100	Delamination
2	40	80	50	500	313	100	Delamination
3	40	80	75	500	208	100	Delamination
4	40	80	100	500	156	100	Delamination
5	60	205	25	293	366	87	NA
6	60	205	35	293	261	87	NA
7	60	205	50	293	183	87	Delamination
8	60	205	85	293	108	87	Delamination
9	60	455	25	132	165	29	Delamination
10	80	80	25	1000	1250	189	NA
11	80	80	35	1000	893	189	NA
12	80	80	50	1000	625	189	NA
13	80	80	80	1000	391	189	NA
14	80	80	100	1000	313	189	Delamination
15	80	80	140	1000	223	189	Delamination
16	80	80	185	1000	169	189	Delamination
17	80	330	25	242	303	83	NA
18	80	330	35	242	216	83	NA
19	80	330	50	242	152	83	NA
20	80	330	80	242	95	83	Warpage
21	100	205	25	488	610	150	Elevated edge and corner
22	100	205	35	488	436	150	Elevated edge and corner
23	100	205	50	488	305	150	Warpage + Elevated edge and corner
24	100	205	85	488	179	150	Warpage + Elevated edge and corner
25	100	205	150	488	102	150	Warpage + Elevated edge and corner
26	100	455	25	220	275	89	NA
27	100	455	35	220	196	89	NA
28	100	455	50	220	137	89	Warpage
29	100	455	85	220	81	89	Warpage + Elevated edge and corner
30	120	330	25	364	455	122	Elevated edge and corner
31	120	330	50	364	227	122	Elevated edge and corner
32	120	330	85	364	134	122	Warpage + Elevated edge and corner
33	120	330	120	364	95	122	Warpage + Elevated edge and corner
34	120	580	25	207	259	92	NA
35	120	580	35	207	185	92	NA
36	120	580	50	207	129	92	Warpage + Elevated edge and corner
37	120	580	90	207	72	92	Warpage + Elevated edge and corner
38	120	830	25	145	181	59	NA
39	120	830	35	145	129	59	NA
40	120	830	55	145	82	59	Warpage
41	120	1080	25	111	139	35	NA
42	120	1080	35	111	99	35	Warpage + Delamination
43	140	455	25	308	385	111	Elevated edge and corner
44	140	455	50	308	192	111	Elevated edge and corner
45	140	455	80	308	120	111	Warpage + Elevated edge and corner
46	140	455	110	308	87	111	Warpage + Elevated edge and corner
47	160	580	25	276	345	108	Elevated edge and corner
48	160	580	50	276	172	108	Elevated edge and corner
49	160	580	75	276	115	108	Warpage + Elevated edge and corner
50	160	580	100	276	86	108	Warpage + Elevated edge and corner
51	160	830	25	193	241	83	NA
52	160	830	35	193	172	83	Warpage + Elevated edge and corner
53	160	830	50	193	120	83	Warpage + Elevated edge and corner
54	160	830	80	193	75	83	Warpage + Elevated edge and corner
55	160	1080	25	148	185	61	NA
56	160	1080	35	148	132	61	NA
57	160	1080	50	148	93	61	Warpage + Delamination
58	160	1080	60	148	77	61	Warpage + Delamination
59	160	1330	25	120	150	37	NA
60	160	1330	35	120	107	37	Warpage + Delamination
61	160	1580	25	101	127	25	NA
62	160	1830	25	87	109	25	NA
63	200	580	25	345	431	118	Elevated edge and corner
64	200	580	50	345	216	118	Elevated edge and corner
65	200	580	80	345	135	118	Warpage + Elevated edge and corner
66	200	580	110	345	98	118	Warpage + Elevated edge and corner
67	200	830	25	241	301	99	Elevated edge and corner
68	200	830	50	241	151	99	Warpage + Elevated edge and corner
69	200	830	95	241	79	99	Warpage + Elevated edge and corner
70	200	1080	25	185	231	82	Elevated edge and corner
71	200	1080	50	185	116	82	Warpage + Elevated edge and corner
72	200	1080	80	185	72	82	Warpage + Elevated edge and corner
73	200	1330	25	150	188	66	NA
74	200	1330	35	150	134	66	Warpage
75	200	1330	65	150	72	66	Warpage + Delamination
76	200	1580	25	127	158	54	NA
77	200	1580	35	127	113	54	Warpage
78	200	1580	50	127	79	54	Warpage + Delamination
79	200	1830	25	109	137	51	NA

Table 3 *Continued*

Cuboid specimen #	P (W)	v (mm/s)	h (μm)	E_L (J/m)	E_V (J/mm^3)	h_{max} (μm)	Defect mode
80	200	1830	35	109	98	51	Warpage + Delamination
81	200	1830	50	109	68	51	Warpage + Delamination
82	200	2080	25	96	120	25	NA
83	200	2330	25	86	107	25	NA
84	240	830	25	289	361	118	Elevated edge and corner
85	240	830	50	289	181	118	Elevated edge and corner
86	240	830	85	289	106	118	Warpage + Elevated edge and corner
87	240	830	115	289	79	118	Warpage + Elevated edge and corner
88	240	1080	25	222	278	99	Elevated edge and corner
89	240	1080	50	222	139	99	Warpage + Elevated edge and corner
90	240	1080	95	222	73	99	Warpage + Elevated edge and corner
91	240	1330	25	180	226	84	Elevated edge and corner
92	240	1330	50	180	113	84	Warpage + Elevated edge and corner
93	240	1330	80	180	70	84	Warpage + Elevated edge and corner
94	240	1580	25	152	190	73	NA
95	240	1580	35	152	136	73	Warpage + Delamination
96	240	1580	50	152	95	73	Warpage + Delamination
97	240	1580	70	152	68	73	Warpage + Delamination
98	240	1830	25	131	164	69	NA
99	240	1830	35	131	117	69	Warpage + Delamination
100	240	1830	50	131	82	69	Warpage + Delamination
101	240	1830	65	131	63	69	Warpage + Delamination
102	240	2080	25	115	144	42	Rough surface
103	240	2080	40	115	90	42	Rough surface
104	240	2330	25	103	129	40	Rough surface
105	240	2330	40	103	80	40	Rough surface

References

[1] Otsuka, K., and Wayman, C. M., 1999, *Shape Memory Materials*, Cambridge University Press, Cambridge.

[2] Shaw, J. A., and Kyriakides, S., 1995, "Thermomechanical Aspects of NiTi," J. Mech. Phys. Solids, **43**(8), pp. 1243–1281.

[3] Hartl, D. J., and Lagoudas, D. C., 2007, "Aerospace Applications of Shape Memory Alloys," Proc. Inst. Mech. Eng. Part G J. Aerosp. Eng., **221** (4), pp. 535–552.

[4] Stoeckel, D., 1990, "Shape Memory Actuators for Automotive Applications," Mater. Des., **11**(6), pp. 302–307.

[5] Petrini, L., and Migliavacca, F., 2011, "Biomedical Applications of Shape Memory Alloys," J. Metall., **2011**, pp. 1–15.

[6] Elahinia, M. H., Hashemi, M., Tabesh, M., and Bhaduri, S. B., 2012, "Manufacturing and Processing of NiTi Implants: A Review," Prog. Mater. Sci., **57**(5), pp. 911–946.

[7] Jani, J. M., Leary, M., Subic, A., and Gibson, M. A., 2014, "A Review of Shape Memory Alloy Research, Applications and Opportunities," Mater. Des., **56**, pp. 1078–1113.

[8] Nematollahi, M., Mehrabi, R., Callejas, M. A., Elahinia, H., and Elahinia, M., 2018, "A Two-Way Architectural Actuator Using NiTi se Wire and SME Spring, in: Active and Passive Smart Structures and Integrated Systems XII," Int. Soc. Opt. Photonics, **10595**, pp. 621–629.

[9] Lin, H., Lin, K., and Chen, Y., 2000, "A Study on the Machining Characteristics of Tini Shape Memory Alloys," J. Mater. Process. Technol., **105**(3), pp. 327–332.

[10] Kaya, E., and Kaya, I., 2019, "A Review on Machining of NiTi Shape Memory Alloys: The Process and Post Process Perspective," Int. J. Adv. Manuf. Technol., **100**(5), pp. 2045–2087.

[11] Manjaiah, M., Narendranath, S., Basavarajappa, S., and Gaitonde, V., 2014, "Wire Electric Discharge Machining Characteristics of Titanium Nickel Shape Memory Alloy," Trans. Nonferrous Met. Soc. China, **24**(10), pp. 3201–3209.

[12] Guo, Y., Klink, A., Fu, C., and Snyder, J., 2013, "Machinability and Surface Integrity of Nitinol Shape Memory Alloy," CIRP Ann., **62**(1), pp. 83–86.

[13] Elahinia, M., Moghaddam, N. S., Andani, M. T., Amerinatanzi, A., Bimber, B. A., and Hamilton, R. F., 2016, "Fabrication of NiTi Through Additive Manufacturing: A Review," Prog. Mater. Sci., **83**, pp. 630–663.

[14] Farber, E., Zhu, J.-N., Popovich, A., and Popovich, V., 2020, "A Review of NiTi Shape Memory Alloy as a Smart Material Produced by Additive Manufacturing," Mater. Today: Proc., **30**(3), pp. 761–767.

[15] King, W. E., Anderson, A. T., Ferencz, R. M., Hodge, N. E., Kamath, C., Khairallah, S. A., and Rubenchik, A. M., 2015, "Laser Powder Bed Fusion Additive Manufacturing of Metals; Physics, Computational, and Materials Challenges," Appl. Phys. Rev., **2**(4), p. 041304.

[16] Sing, S., and Yeong, W., 2020, "Laser Powder Bed Fusion for Metal Additive Manufacturing: Perspectives on Recent Developments," Virtual Phys. Prototyp., **15**(3), pp. 359–370.

[17] Oliveira, J. P., LaLonde, A., and Ma, J., 2020, "Processing Parameters in Laser Powder Bed Fusion Metal Additive Manufacturing," Mater. Des., **193**, p. 108762.

[18] Mahmoudi, M., Tapia, G., Franco, B., Ma, J., Arroyave, R., Karaman, I., and Elwany, A., 2018, "On the Printability and Transformation Behavior of Nickel-Titanium Shape Memory Alloys Fabricated Using Laser Powder-Bed Fusion Additive Manufacturing," J. Manuf. Processes, **35**, pp. 672–680.

[19] Xue, L., Atli, K., Picak, S., Zhang, C., Zhang, B., Elwany, A., Arroyave, R., and Karaman, I., 2021, "Controlling Martensitic Transformation Characteristics in Defect-Free NiTi Shape Memory Alloys Fabricated Using Laser Powder Bed Fusion and a Process Optimization Framework," Acta Mater., **215**, p. 117017.

[20] Zhu, J.-N., Borisov, E., Liang, X., Farber, E., Hermans, M., and Popovich, V., 2021, "Predictive Analytical Modelling and Experimental Validation of Processing Maps in Additive Manufacturing of Nitinol Alloys," Addit. Manuf., **38**, p. 101802.

[21] Mehrpouya, M., Gisario, A., Rahimzadeh, A., Nematollahi, M., Baghbaderani, K. S., and Elahinia, M., 2019, "A Prediction Model for Finding the Optimal Laser Parameters in Additive Manufacturing of NiTi Shape Memory Alloy," Int. J. Adv. Manuf. Technol., **105**(11), pp. 4691–4699.

[22] Saedi, S., Moghaddam, N. S., Amerinatanzi, A., Elahinia, M., and Karaca, H. E., 2018, "On the Effects of Selective Laser Melting Process Parameters on Microstructure and Thermomechanical Response of Ni-Rich NiTi," Acta Mater., **144**, pp. 552–560.

[23] Zhang, Q., Hao, S., Liu, Y., Xiong, Z., Guo, W., Yang, Y., Ren, Y., Cui, L., Ren, L., and Zhang, Z., 2020, "The Microstructure of a Selective Laser Melting (SLM)-Fabricated NiTi Shape Memory Alloy With Superior Tensile Property and Shape Memory Recoverability," Appl. Mater. Today, **19**, p. 100547.

[24] Dadbakhsh, S., Vrancken, B., Kruth, J.-P., Luyten, J., and Van Humbeeck, J., 2016, "Texture and Anisotropy in Selective Laser Melting of NiTi Alloy," Mater. Sci. Eng. A, **650**, pp. 225–232.

[25] Saedi, S., Turabi, A. S., Andani, M. T., Moghaddam, N. S., Elahinia, M., and Karaca, H. E., 2017, "Texture, Aging, and Superelasticity of Selective Laser Melting Fabricated Ni-Rich NiTi Alloys," Mater. Sci. Eng. A, **686**, pp. 1–10.

[26] Wang, X., Yu, J., Liu, J., Chen, L., Yang, Q., Wei, H., Sun, J., et al.et al., 2020, "Effect of Process Parameters on the Phase Transformation Behavior and Tensile Properties of NiTi Shape Memory Alloys Fabricated by Selective Laser Melting," Addit. Manuf., **36**, p. 101545.

[27] Moghaddam, N. S., Saghaian, S. E., Amerinatanzi, A., Ibrahim, H., Li, P., Toker, G. P., Karaca, H. E., and Elahinia, M., 2018, "Anisotropic Tensile and Actuation Properties of NiTi Fabricated With Selective Laser Melting," Mater. Sci. Eng. A, **724**, pp. 220–230.

[28] Zhao, C., Liang, H., Luo, S., Yang, J., and Wang, Z., 2020, "The Effect of Energy Input on Reaction, Phase Transition and Shape Memory Effect of NiTi Alloy by Selective Laser Melting," J. Alloys Compd., **817**, p. 153288.

[29] Yang, Y., Zhan, J., Sun, Z., Wang, H., Lin, J., Liu, Y., and Zhang, L., 2019, "Evolution of Functional Properties Realized by Increasing Laser Scanning Speed for the Selective Laser Melting Fabricated NiTi Alloy," J. Alloys Compd., **804**, pp. 220–229.

[30] Saedi, S., Saghaian, S. E., Jahadakbar, A., Moghaddam, N. S., Andani, M. T., Saghaian, S. M., Lu, Y. C., Elahinia, M., and Karaca, H. E., 2018, "Shape Memory Response of Porous NiTi Shape Memory Alloys Fabricated by Selective Laser Melting," J. Mater. Sci.: Mater. Med., **29**(4), pp. 1–12.

[31] Andani, M. T., Saedi, S., Turabi, A. S., Karamooz, M., Haberland, C., Karaca, H. E., and Elahinia, M., 2017, "Mechanical and Shape Memory Properties of Porous Ni50. 1Ti49. 9 Alloys Manufactured by Selective Laser Melting," J. Mech. Behav. Biomed. Mater., **68**, pp. 224–231.

[32] Gan, J., Duan, L., Li, F., Che, Y., Zhou, Y., Wen, S., and Yan, C., 2021, "Effect of Laser Energy Density on the Evolution of Ni4Ti3 Precipitate and Property of NiTi Shape Memory Alloys Prepared by Selective Laser Melting," J. Alloys Compd., **869**, p. 159338.

[33] Saedi, S., Turabi, A. S., Andani, M. T., Haberland, C., Karaca, H., and Elahinia, M., 2016, "The Influence of Heat Treatment on the Thermomechanical Response

of Ni-Rich NiTi Alloys Manufactured by Selective Laser Melting," J. Alloys Compd., **677**, pp. 204–210.
[34] Khoo, Z. X., An, J., Chua, C. K., Shen, Y. F., Kuo, C. N., and Liu, Y., 2019, "Effect of Heat Treatment on Repetitively Scanned slm NiTi Shape Memory Alloy," Materials, **12**(1), p. 77.
[35] Chen, X., Liu, K., Guo, W., Gangil, N., Siddiquee, A. N., and Konovalov, S., 2019, "The Fabrication of NiTi Shape Memory Alloy by Selective Laser Melting: A Review," Rapid Prototyp. J., **25**(8), pp. 1421–1432.
[36] Safaei, K., Abedi, H., Nematollahi, M., Kordizadeh, F., Dabbaghi, H., Bayati, P., Javanbakht, R., Jahadakbar, A., Elahinia, M., and Poorganji, B., 2021, "Additive Manufacturing of NiTi Shape Memory Alloy for Biomedical Applications: Review of the LPBF Process Ecosystem," JOM, **73**(12), pp. 3771–3786.
[37] Frenzel, J., George, E. P., Dlouhy, A., Somsen, C., Wagner, M.-X., and Eggeler, G., 2010, "Influence of Ni on Martensitic Phase Transformations in NiTi Shape Memory Alloys," Acta Mater., **58**(9), pp. 3444–3458.
[38] Shi, X., Cui, L., Jiang, D., Yu, C., Guo, F., Yu, M., Ren, Y., and Liu, Y., 2014, "Grain Size Effect on the r-Phase Transformation of Nanocrystalline NiTi Shape Memory Alloys," J. Mater. Sci., **49**(13), pp. 4643–4647.
[39] Haberland, C., Elahinia, M., Walker, J. M., Meier, H., and Frenzel, J., 2014, "On the Development of High Quality NiTi Shape Memory and Pseudoelastic Parts by Additive Manufacturing," Smart Mater. Struct., **23**(10), p. 104002.
[40] Dadbakhsh, S., Speirs, M., Kruth, J.-P., Schrooten, J., Luyten, J., and Van Humbeeck, J., 2014, "Effect of SLM Parameters on Transformation Temperatures of Shape Memory Nickel Titanium Parts," Adv. Eng. Mater., **16**(9), pp. 1140–1146.
[41] Bormann, T., Müller, B., Schinhammer, M., Kessler, A., Thalmann, P., and de Wild, M., 2014, "Microstructure of Selective Laser Melted Nickel–Titanium," Mater. Charact., **94**, pp. 189–202.
[42] Franco, B., Ma, J., Loveall, B., Tapia, G., Karayagiz, K., Liu, J., Elwany, A., Arroyave, R., and Karaman, I., 2017, "A Sensory Material Approach for Reducing Variability in Additively Manufactured Metal Parts," Sci. Rep., **7**(1), pp. 1–12.
[43] Ma, J., Franco, B., Tapia, G., Karayagiz, K., Johnson, L., Liu, J., Arroyave, R., Karaman, I., and Elwany, A., 2017, "Spatial Control of Functional Response in 4D-Printed Active Metallic Structures," Sci. Rep., **7**(1), pp. 1–8.
[44] Eagar, T. W., Tsai, N. S., 1983, "Temperature Fields Produced by Traveling Distributed Heat Sources," Weld. J., **62**(12), pp. 346–355.
[45] Seede, R., Shoukr, D., Zhang, B., Whitt, A., Gibbons, S., Flater, P., Elwany, A., Arroyave, R., and Karaman, I., 2020, "An Ultra-High Strength Martensitic Steel Fabricated Using Selective Laser Melting Additive Manufacturing: Densification, Microstructure, and Mechanical Properties," Acta Mater., **186**, pp. 199–214.
[46] Yadroitsev, I., Gusarov, A., Yadroitsava, I., and Smurov, I., 2010, "Single Track Formation in Selective Laser Melting of Metal Powders," J. Mater. Process. Technol., **210**(12), pp. 1624–1631.
[47] Gu, D., and Shen, Y., 2009, "Balling Phenomena in Direct Laser Sintering of Stainless Steel Powder: Metallurgical Mechanisms and Control Methods," Mater. Des., **30**(8), pp. 2903–2910.
[48] Sun, S.-H., Ishimoto, T., Hagihara, K., Tsutsumi, Y., Hanawa, T., and Nakano, T., 2019, "Excellent Mechanical and Corrosion Properties of Austenitic Stainless Steel With a Unique Crystallographic Lamellar Microstructure via Selective Laser Melting," Scr. Mater., **159**, pp. 89–93.
[49] Bobel, A., Hector, L. G., Jr., Chelladurai, I., Sachdev, A. K., Brown, T., Poling, W. A., Kubic, R., et al., 2019, "In Situ Synchrotron X-ray Imaging of 4140 Steel Laser Powder Bed Fusion," Materialia, **6**, p. 100306.
[50] Campanelli, S., Contuzzi, N., Posa, P., and Angelastro, A., 2019, "Study of the Aging Treatment on Selective Laser Melted Maraging 300 Steel," Mater. Res. Express, **6**(6), p. 066580.
[51] Guo, W., Sun, Z., Yang, Y., Wang, X., Xiong, Z., Li, Z., Wang, C., et al., 2020, "Study on the Junction Zone of NiTi Shape Memory Alloy Produced by Selective Laser Melting via a Stripe Scanning Strategy," Intermetallics, **126**, p. 106947.
[52] Promoppatum, P., and Yao, S.-C., 2020, "Influence of Scanning Length and Energy Input on Residual Stress Reduction in Metal Additive Manufacturing: Numerical and Experimental Studies," J. Manuf. Processes, **49**, pp. 247–259.
[53] Fu, J., Hu, Z., Song, X., Zhai, W., Long, Y., Li, H., and Fu, M., 2020, "Micro Selective Laser Melting of NiTi Shape Memory Alloy: Defects, Microstructures and Thermal/Mechanical Properties," Opt. Laser Technol., **131**, p. 106374.
[54] Noble, W. S., 2006, "What is a Support Vector Machine?," Nat. Biotechnol., **24**(12), pp. 1565–1567.
[55] Suykens, J. A., and Vandewalle, J., 1999, "Least Squares Support Vector Machine Classifiers," Neural Process. Lett., **9**(3), pp. 293–300.
[56] Hussain, M., Wajid, S. K., Elzaart, A., and Berbar, M., 2011, "A Comparison of SVM Kernel Functions for Breast Cancer Detection," Proceedings of the 2011 Eighth International Conference Computer Graphics, Imaging and Visualization, Singapore, Aug. 17–19.
[57] Chawla, N. V., Bowyer, K. W., Hall, L. O., and Kegelmeyer, W. P., 2002, "Smote: Synthetic Minority Over-Sampling Technique," J. Artif. Intell. Res., **16**, pp. 321–357.
[58] King, W. E., Barth, H. D., Castillo, V. M., Gallegos, G. F., Gibbs, J. W., Hahn, D. E., Kamath, C., and Rubenchik, A. M., 2014, "Observation of Keyhole-Mode Laser Melting in Laser Powder-Bed Fusion Additive Manufacturing," J. Mater. Process. Technol., **214**(12), pp. 2915–2925.
[59] Strano, G., Hao, L., Everson, R. M., and Evans, K. E., 2013, "Surface Roughness Analysis, Modelling and Prediction in Selective Laser Melting," J. Mater. Process. Technol., **213**(4), pp. 589–597.
[60] Zhao, Z., Li, L., Tan, L., Bai, P., Li, J., Wu, L., Liao, H., and Cheng, Y., 2018, "Simulation of Stress Field During the Selective Laser Melting Process of the Nickel-Based Superalloy, gh4169," Materials, **11** (9), p. 1525.
[61] Gajera, H. M., and Dave, K. G., 2018, "Experimental Investigation and Optimization of Direct Metal Laser Sintering Process for Shrinkage Rate Using cl50ws Material," Mater. Today: Proc., **5**(9), pp. 19126–19135.
[62] Sames, W. J., List, F., Pannala, S., Dehoff, R. R., and Babu, S. S., 2016, "The Metallurgy and Processing Science of Metal Additive Manufacturing," Int. Mater. Rev., **61**(5), pp. 315–360.
[63] Tang, C., Le, K. Q., and Wong, C. H., 2020, "Physics of Humping Formation in Laser Powder Bed Fusion," Int. J. Heat Mass Transfer, **149**, p. 119172.
[64] Matache, G., Vladut, M., Paraschiv, A., and Condruz, R. M., 2020, "Edge and Corner Effects in Selective Laser Melting of in 625 Alloy," Manuf. Rev., **7**(8), pp. 1–7.
[65] Yasa, E., Deckers, J., Craeghs, T., Badrossamay, M., and Kruth, J.-P., 2009, "Investigation on Occurrence of Elevated Edges in Selective Laser Melting," International Solid Freeform Fabrication Symposium, Austin, TX, Aug. 3–5, pp. 673–685.